

Potential of Recurrence Metrics from Sentinel-1 Time Series for Deforestation Mapping

Felix Cremer¹, Mikhail Urbazaev¹, *Member, IEEE*, José Cortés, John Truckenbrodt, Christiane Schmullius, and Christian Thiel¹

Abstract—The REDD+ framework requires accurate estimates of deforestation. These are derived by ground measurements supported by methods based on remote sensing data to automatically detect and delineate deforestations over large areas. In particular, in the tropics, optical data is seldom available due to cloud cover. As synthetic aperture radar (SAR) data overcomes this limitation, we performed a separability analysis of two statistical metrics based on the Sentinel-1 SAR backscatter over forested and deforested areas. We compared the range between the 5th and 95th temporal percentiles (PRange) and the recurrence quantification analysis (RQA) Trend metric. Unlike the PRange, the RQA Trend considers the temporal order of the SAR data acquisitions, thus contrasting between dropping backscatter signals and yearly seasonalities. This enables the estimation of the timing of deforestation events. We assessed the impact of polarization, acquisition orbit, and despeckling on the separability between forested and deforested areas and between different deforestation timings for two test sites in Mexico. We found that the choice of the orbit impacts the detectability of deforestation. In all cases, VH data showed a higher separability between forest and deforestations than VV data. The PRange slightly outperformed RQA Trend in the separation between forest and deforestation. However, the RQA Trend exceeded the PRange in the separation between different deforestation timings. In this study, C-Band backscatter data was used, although it is commonly not considered as the most suitable SAR dataset for forestry applications. Nevertheless, our approach shows the potential of dense C-Band backscatter time series to support the REDD+ framework.

Index Terms—Forestry, radar remote sensing, synthetic aperture radar, time series analysis.

Manuscript received February 28, 2020; revised July 29, 2020; accepted August 10, 2020. Date of publication September 3, 2020; date of current version September 18, 2020. This work was supported in part by DLR in the Sentinel4REDD project under Grant FKZ:50EE1540 and in part by DFG in the HyperSense project under Grant TH 1435/4-1. The work of Felix Cremer was supported by the ESDL Early Adopter call. The work of Mikhail Urbazaev was supported in part by the 2017–2018 Belmont Forum and BiodivERSa joint call for research proposals, under the BiodivScen ERA-Net COFUND programme, and in part by the funding organisation the German Federal Ministry of Education and Research (BMBF) under Grant 01LC1808A. (*Corresponding author: Felix Cremer.*)

Felix Cremer and John Truckenbrodt are with the German Aerospace Center, Institute of Data Science, 07745 Jena, Germany and also with the Chair of Earth Observation, Friedrich-Schiller University, 07743 Jena, Germany (e-mail: felix.cremer@uni-jena.de; john.truckenbrodt@uni-jena.de).

Mikhail Urbazaev and Christiane Schmullius are with the Chair of Earth Observation, Friedrich-Schiller University, 07743 Jena, Germany (e-mail: mikhail.urbazaev@uni-jena.de; c.schmullius@uni-jena.de).

José Cortés is with the GIScience Group, Friedrich-Schiller University, 07743 Jena, Germany (e-mail: Jose.cortes@uni-jena.de).

Christian Thiel is with the German Aerospace Center, Institute of Data Science, 07743 Jena, Germany (e-mail: Christian.Thiel@uni-jena.de).

Digital Object Identifier 10.1109/JSTARS.2020.3019333

I. INTRODUCTION

THE tropical forest ecosystems stabilize the world climate [1] and protect global biodiversity [2]. In the last decades, remote sensing technologies have played a substantial role by providing consistent, reliable, and timely information about forest cover and forest cover changes. Operational forest/nonforest and forest cover change products are mainly based on optical sensors [3]. However, clouds obstruct optical imagery, especially in the tropics during the rainy season. Alternatively, forest cover and forest cover change can be mapped using cloud penetrating synthetic aperture radar (SAR) data. These maps are mostly based on L-Band SAR data because the longer wavelength penetrates deeper into the forest structure [4] or on X-Band SAR interferometry data [5]. Unfortunately, there exists no freely available global SAR L-Band time series dataset. This will change in the near future once the NASA-ISRO L-Band sensor NISAR is launched. The European Copernicus Programme provides a global SAR C-Band dataset with a high spatial (ca. 10 m) and temporal resolution (six days).

Since SAR is sensitive to geometrical and dielectric properties of a target, the backscattered signal of the single time steps can vary considerably. As a result, vegetation maps based on mono-temporal SAR data might show high variance. The separability between the forest cover and the bare soil in C-Band data can be enhanced by time series data. This can be achieved by reducing the effects of environmental conditions (e.g., rain, wind, etc.) on the SAR signal.

Current approaches that use Sentinel-1 backscatter data to detect deforestations can be summarized in two different groups. One group represents the approaches that use the Sentinel-1 time series as a stream of single images or a stream of a few images. Bouvet *et al.* [6] used the emerging and disappearing radar shadow effects due to the logging of tall trees to detect the edges of deforested areas. Since the SAR shadow is a geometrical effect, it is persistent over time and therefore not prone to seasonal effects. This method detects edges only in the viewing direction of the satellite and therefore works best when it is used on ascending and descending acquisition orbits in combination to reconstruct the full deforestation polygons. Rüetschi *et al.* [7] used the difference of the average of five images before and after a storm event respectively to detect windthrow areas. Then they apply a threshold on the backscatter difference and on the number of pixels per detection to derive affected areas. This method achieves a good detection rate, but it cannot delineate the areas and thus is not suitable for area estimations.

Another group of methods use the time series during a preparation time span to derive for every pixel what is to be expected and to then use every new acquisition to update whether deforestations appear. Shimizu *et al.* [8] used a harmonic model to derive indices which describe the seasonality of the Sentinel-1 time series. These indices are then used to train a random forest model which is updated on every succeeding time step. By using the harmonic model, they are incorporating the seasonality of the Sentinel-1 time series. They showed that their method's accuracy is sensitive to the selected threshold for disturbance from the random forest model and also to the minimum mapping unit. Reiche *et al.* [9] used Bayesian updating on deforestation probabilities to derive a possible deforestation on every acquisition. They spatially normalized the pixel time series to decrease the seasonality of the Sentinel-1 time series. Spatial normalization is conducted by dividing the value of one pixel by the 95th percentile of the neighborhood. Then they used the first year of their sensing period to derive local forest/nonforest distributions. With these F/NF distributions, they converted the pixel value in a nonforest probability and used the Bayesian theorem to update their nonforest probability in every pixel. When the nonforest probability exceeds a certain threshold, the time step was marked as a possible deforestation which was confirmed or declined on the next step. Hirschmuggl *et al.* [10] used a threshold on the temporal coefficient of variation to derive changing pixels. They flagged these pixels as deforestation if they have a negative backscatter trend. The backscatter trend was computed as the difference of the average backscatter of the first three images of the time series and the average of the last three images of the time series. They showed that all deforestations larger than 1 ha have been detected at least partially.

In this article, we examine two statistical metrics calculated from Sentinel-1 C-Band SAR backscatter time series data on their performance to separate forested and deforested areas. One statistical metric is the range between the 5th and 95th percentiles (PRange). This metric was proposed by [11], but its applicability to separating forest and deforestation has not been investigated yet.

Another statistical metric can be derived from recurrence quantification analysis (RQA) [12]. This is a technique to derive multitemporal statistics by considering the inherent order of a time series. RQA is based on recurrence plots (RPs) which have been introduced by [13]. So far, this technique has only been applied to optical remote sensing time series. RQA has been used to investigate temporal dynamics of AVHRR NDVI time series between 1981 and 2003 [14] and of RQA MODIS EVI data for the years 2000–2013 [15]. They both showed that the RQA metrics can be used to differentiate between the predictability of the time series for different land covers. This is the first time that the RQA metrics are calculated for SAR time series. The rest of this article is organized as follows. In Section II, we describe RPs and RQA. In Section III, we describe the results of the comparison of the PRange and the RQA Trend metric. Section IV discusses the results and Section V summarizes the results of the article.

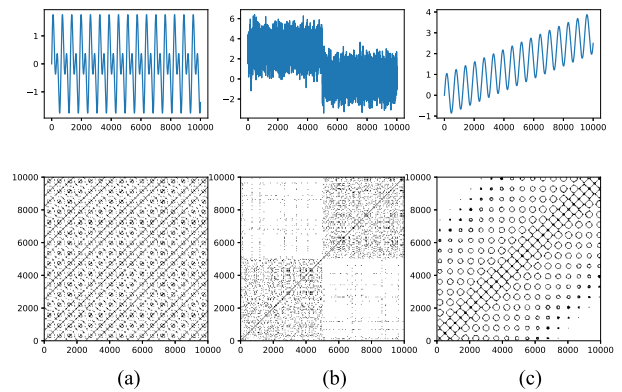


Fig. 1. Recurrence plots for (a) the sum of two sine waves with different frequencies, (b) a step function with noise, and (c) a sine wave with trend.

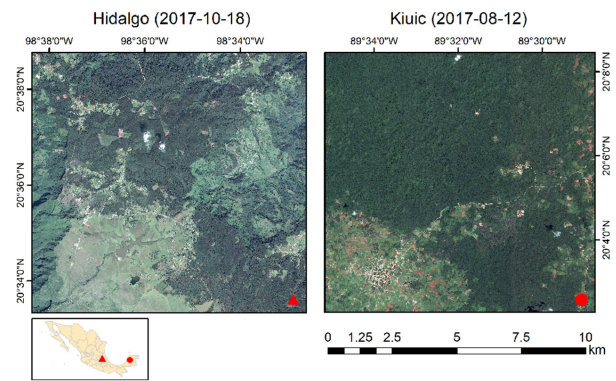


Fig. 2. Pléiades data in October 2017 of the two test sites, which are located in Mexico and are dominated by temperate forests (Hidalgo) and tropical dry forest (Kiuic).

II. METHODS

A. Multitemporal Metrics

RPs are a method to visualize the recurrences of a signal. From these patterns, we can compute RQA metrics to quantify the number and duration of recurrences. The RP of a time series x_i is defined as follows:

$$R_{i,j} = \theta(\epsilon - |x_i - x_j|), i, j = 1, \dots, N \quad (1)$$

where ϵ is a threshold value that indicates up to which distance two time steps are viewed as similar. θ is the Heaviside function which sets everything below zero to zero and every positive value to one. N is the number of elements of the signal. This computation leads to a square matrix with black dots where the time steps are similar to each other. The main diagonal is always black because every time step is similar to itself. Fig. 1(a) shows examples of RPs of a sum of two sine waves with different frequencies, Fig. 1(b) shows a step function from three to zero with an overlaid white noise with standard deviation of 1, and Fig. 3(c) shows a sine wave with overlaying trend. For the composition of two sine curves, we see a regular pattern with distinguished diagonals which indicate the frequencies of the subsignals. In the noisy step function, four distinct quadrants

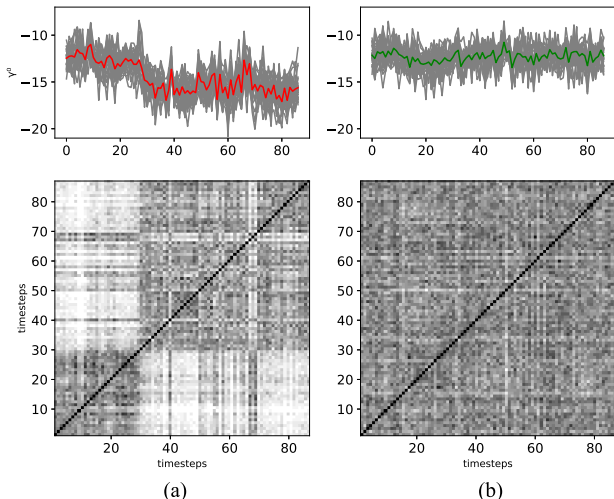


Fig. 3. Recurrence plots for 25 pixels of deforestation (left) and stable forest (right). The gray lines are each pixel’s time series and the colored line is their respective mean.

can be found in the RP. In the two quadrants near the main diagonal, every point is randomly similar to other points with a high probability. In the other two quadrants, the probability that two points are similar to a point in the other part of the step function is low. In the third example, a clear pattern can be seen, but these patterns fade out to the edge of the RP. This is due to the difference of the values at the beginning and the end of the time series. Therefore, we can use this pattern as an indicator for a trend in the time series.

These visual patterns can be quantified using RQA [12], [16]. The simplest measure is the recurrence rate (RR) which is the number of recurrences divided by the squared number of elements in the signal. It measures the density of the recurrence points in an RP. In the following, we use the Trend metric for separability analysis. It is defined as

$$\text{TREND} = \frac{\sum_{\tau=1}^{\tilde{N}} (\tau - \tilde{N}/2) (\text{RR}_{\tau} - \langle \text{RR}_{\tau} \rangle)}{\sum_{\tau=1}^{\tilde{N}} (\tau - \tilde{N}/2)}. \quad (2)$$

Hereby, \tilde{N} is the number of time steps and RR_i is the number of recurrent values on the i th diagonal. It represents the linear regression coefficient over the RR of the diagonals in comparison to their distance to the main diagonal. It indicates whether the process is drifting or not. All RQA results have been produced with the Julia RecurrenceAnalysis.jl package [17].

The percentile range is proposed by [11] as an approach to detect deforestation. The PRange is defined as the difference between the 95th and 5th percentile to mitigate the influence of massive outliers

$$\text{PRange} = P_{95} - P_5. \quad (3)$$

As the span of the temporal values, it is highly influenced by fluctuations in the time series. It captures the general variability of a time series. Since deforestations correspond to a drop in backscatter, the PRange can be used to detect deforestations [11].

B. Receiver Operator Characteristics

A common method to evaluate binary classifiers is to compare the receiver operating characteristic (ROC) curves. The ROC curve plots the true positive rate (correctly identified deforestation) against the false positive rate (incorrectly identified deforestation) as the decision threshold changes. The unitary slope line represents a random classification, whereas points above it are results better than random, and points below are results that are worse than random. A measure of a model’s overall performance can be given by the area under the curve (AUC) of the ROC curve. High values of AUC represent strong overall performance. An AUC of 0.5 is equivalent to a random classification, and an AUC of 1 represents perfect classification.

III. EXPERIMENTAL RESULTS

A. Test Sites

We tested the separability between forested and deforested areas over two study sites in Mexico which are shown in Fig. 2. The first study site is located in the municipality of Zacualtipan, state of Hidalgo, and covered by mountain cloud forest, pine forest, and pine-oak forests [18]. The second study site is situated on the Yucatan peninsula near the biocultural reserve of Kaxil Kiuic and is covered by tropical dry forests [19]. Each of the study sites extends over an area of 10×10 km.

The Hidalgo site is a mountainous region characterized by a minimum elevation of about 1125 m and a maximum elevation of 2238 m with a mean slope of 16° [20]. The regional climate is humid-temperate characterized by a mean annual temperature of 13°C and around 2000 mm of precipitation [18] with a pronounced rainy season between June and October, when more than 80% of the total annual precipitation occur [21]. The management strategies have focused on development of even-aged stands of *Pinus patula*, which is a highly productive fast growing subtropical species broadly used for forest plantations [22]. AGB of the pine-managed forest stands (3–28 years old) ranges between 0.5 and 170t ha^{-1} , while primeval old-growth forests reach a maximum AGB of 290t ha^{-1} [23].

The second study site, Kiuic, is located on flat terrain with an average elevation of 94 m and a mean slope of 9° . The regional climate is tropical subhumid with slightly higher air temperatures in summer than in winter. The average annual temperature between 2013 and 2017 was 27°C [24]. Average annual precipitation ranges from 1000 to 1100 mm. The period between May and November is characterized by pronounced rainfall, and the relatively dry period extends between December and April [24]. The forests in the north-western part of the Yucatan peninsula have experienced slash-and-burn agriculture for 2000 years, resulting in forest patches at different succession stages [25]. The Kiuic site is located in a private protected area and mainly covered by dry semideciduous tropical forests, where more than 50% of tree species shed their leaves during the dry season [19]. The average aboveground biomass in the area ranges between 110 and 180t ha^{-1} [19].

Both study sites are part of the network of intensive carbon monitoring sites in Mexico [26], where forest carbon fluxes are measured at different spatial scales (e.g., permanent plots, eddy covariance towers, LiDAR remote sensing, and carbon dynamics models) [26].

B. Data and Preprocessing

We preprocessed the Sentinel-1 GRD datasets after [27] and resampled them to a 10×10 m pixel spacing. The preprocessing consists of the following steps: Thermal noise removal, border noise removal, calibration, terrain flattening, and terrain correction. The orthorectification is based on the orbit state vectors and the 30 m SRTM digital elevation model [28]. The preprocessing also included radiometric terrain flattening after [29], which results in γ^0 backscatter values. Areas featuring layover, foreshortening, and radar shadow were masked out. All images were coregistered in the DEM geometry after geocoding to achieve a subpixel coregistration precision which is of eminent importance when a time series analysis is applied. We preprocessed the SAR data with the SNAP software [30] in version 6 and the Python package pyroSAR [31] and handled it afterwards in the Earth System Data Lab Julia package [32].

We reduced speckle and other unwanted short-term changes of the data using the nonspatial temporal filter described in [33]. The filter is based on the empirical mode decomposition, a data adaptive alternative to the Fourier transform, which can handle nonstationary data. Each pixel is separately decomposed into subsignals of different temporal frequencies. In order to reduce speckle, the two subsignals with the highest temporal frequencies are removed. This results in a nonparametric image transform that fully preserves the geometric resolution and has a similar speckle suppression as the spatio-temporal filter proposed by [34] with a 5×5 filter window [33].

We manually derived reference forest and deforestation areas by comparing Pléiades data acquired in September 2016, October 2017, and July 2018. We delimited three classes: Forest over the entire time, deforestation between September 2016 and October 2017, and deforestation between October 2017 and July 2018. We computed the RQA Trend metric from the time series between March 2017 and March 2019 to ensure a high detection rate of deforestations in the time series and to allow for a ramp up and ramp down phase for the RQA metric.

C. RQA Trend and PRange results

The RPs for Sentinel-1 time series over exemplary forested and deforested areas can be seen in Fig. 3. The upper figures show the time series of VH backscatter over 25 randomly sampled pixels of a deforested area (a) and a stable forest (b) with the mean backscatter as shown in red and green, respectively. The lower figures show the grayscale of the corresponding RPs. The darker a point in the RP, the more the pixels have similar time steps. Hence, at black points, every pixel shows a similarity of the two time steps and at white points, no pixel shows it. There is a clear drop in the backscatter time series for the pixels in the deforested area. The RP represents this change as tow large white areas in the corner similar to the example in Fig. 1(b).

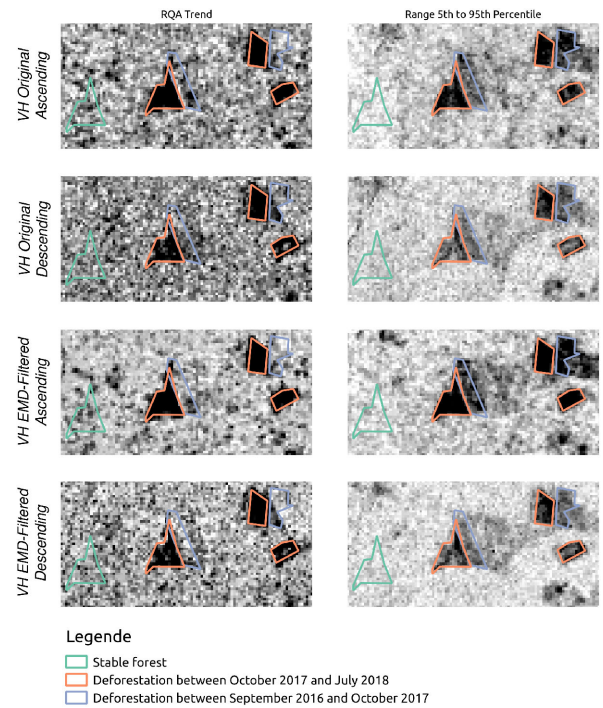


Fig. 4. Visual comparison between RQA Trend and PRange. The red polygons are deforestations between September 2016 and October 2017 and the violet polygons are deforestations between October 2017 and July 2018. These polygons were selected from yearly VHR Pléiades data.

The time series of the deforested area shows seasonality with an amplitude as high as the forest time series for short time periods, visible in the RP as small dark stripes in the white corner.

In the forest, the time series is stable with small backscatter differences between every time step. This is visible in the RP as random noise.

Fig. 4 shows the RQA Trend and the PRange computed from original and EMD-filtered VH data from March 2017 to March 2019. The red polygons represent deforested areas between September 2016 and October 2017 and the violet ones are deforested areas between October 2017 and July 2018. The later deforestations, which are completely in our sensing period, are distinctly visible as clear black areas in the RQA Trend metric and in the PRange metric for VH ascending data. To reduce the effect of speckle and short-term changes in the data, we used the EMD filter. The EMD filter reduces the temporal variance in the time series and thereby enhances the difference between forest and deforestation areas. The PRange metric benefits especially from the temporal denoising by the EMD filter. The earlier deforestations are also partly visible because the Sentinel-1 backscatter signal of the deforested areas shows a yearly seasonality with a maximum amplitude similar to the amplitude of the forest backscatter signal which leads to a high PRange value. The VH backscatter data shows a higher contrast than VV backscatter data between deforestation areas and stable forest. We noticed also a difference between the ascending and the descending orbits. The deforestation areas are better visible in the ascending orbits in both temporal metrics. In the RQA

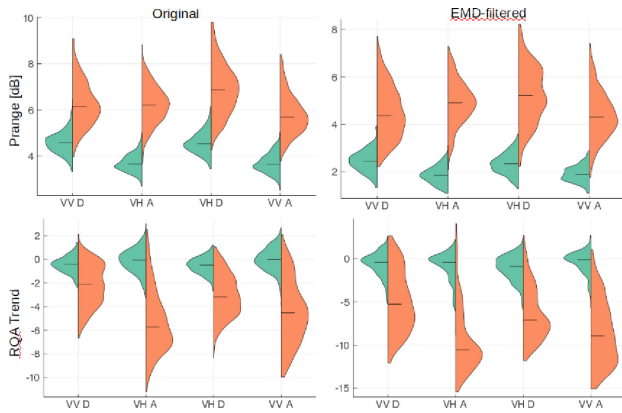


Fig. 5. Violin plots of the Hidalgo test site of deforestation (right) and a stable forest area (left) of similar size for the original and EMD-filtered data for the ascending and descending stacks in both polarizations. The line in the violin is the median of the data.

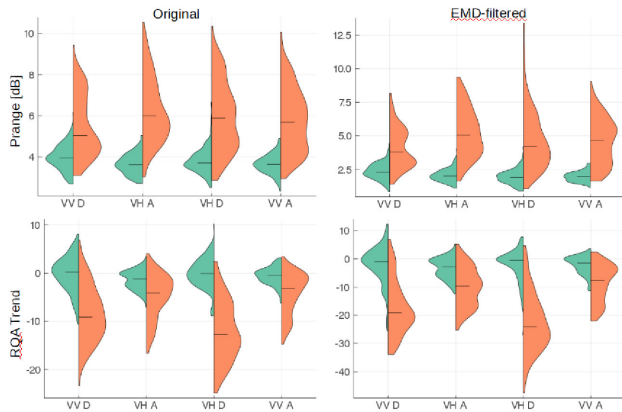


Fig. 6. Violin plots of the Kiuiuc test site of deforestation (right) and a stable forest area (left) of similar size for the original and EMD-filtered data for the ascending and descending stacks in both polarizations.

Trend metric, the old deforestation areas are more distinguishable from the new deforestation areas than in the PRRange metric. This is consistent over all combinations of polarizations and filter application.

D. Separability Analysis

We compare the histograms in the violin plots (Figs. 5 and 6). Deforestation areas are shown in orange and the stable forest areas in green. In Hidalgo, the pixels over stable forests have a narrow distribution compared to the deforestation pixels. The least overlap between the histograms is visible in the VH ascending PRRange data. The EMD-filter further reduces the histogram overlap for the PRRange in the VH data by lowering the overall PRRange values, especially pronounced for the stable forest areas. The EMD-filtered VH ascending data achieves a nearly complete separation between the stable forest and the deforestation areas. The RQA Trend histograms of the deforested areas are rather stretched and thus overlap with the histograms of the stable forest areas.

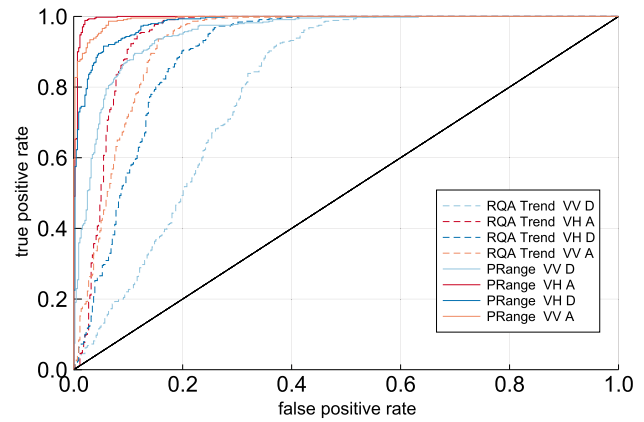


Fig. 7. ROC for the labeling of deforestation against stable forest for the PRRange and RQA Trend in Hidalgo.

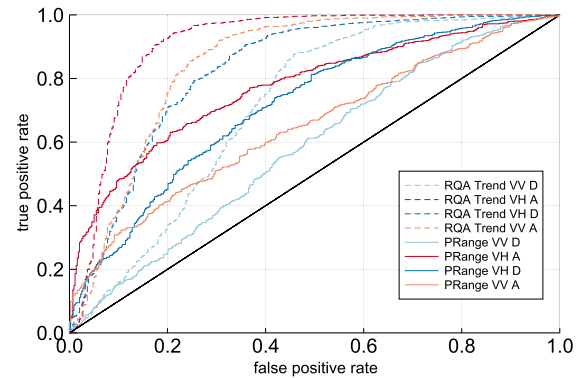


Fig. 8. ROC for the labeling of new deforestation against old deforestation for the PRRange and RQA Trend.

Fig. 6 shows similar plots for the tropical dry forest in Kiuiuc. The backscatter variability of the stable forest areas is higher than that in the Hidalgo test site. Therefore, the separability is overall worse. The EMD-filter smooths the backscatter time series, thus improving separability. For the RQA Trend metric, the best separability is achieved in the VH descending data and for the PRRange in the VH ascending data.

We used the ROC as shown in Fig. 7 for Hidalgo to quantify the separability between forest and deforestation. For every polarization and orbit combination, the PRRange separates better between deforestation and stable forest than the RQA Trend metric. The ranking of the polarizations and orbit combinations is the same in both metrics, namely VH ascending, VH descending, VV ascending, and VV descending. VH descending and VV ascending perform similarly in the PRRange metric. Table I shows the corresponding AUC values with the minima and maxima of the comparison in bold.

For the same comparison of the separation between old and new deforestation, see Fig. 8. The RQA Trend metric shows higher separation between old and new deforestation. For the PRRange, the ranking is the same as in the separation between forest and new deforestation. For the RQA Trend metric, the VH

TABLE I
AREA UNDER CURVE VALUES

	VH A	VH D	VV A	VV D
Stable forest vs new deforestation Hidalgo				
PRange	0.996	0.982	0.993	0.951
RQA Trend	0.944	0.896	0.927	0.795
PRange EMD-filtered	0.998	0.99	0.992	0.972
RQA Trend EMD-filtered	0.951	0.925	0.975	0.843
New deforestation vs old deforestation Hidalgo				
PRange	0.771	0.716	0.649	0.583
RQA Trend	0.91	0.827	0.848	0.711
PRange EMD-filtered	0.829	0.771	0.686	0.598
RQA Trend EMD-filtered	0.916	0.859	0.875	0.757
Stable forest vs new deforestation Kiuc				
PRange	0.964	0.894	0.924	0.82
RQA Trend	0.735	0.953	0.764	0.88
PRange EMD-filtered	0.973	0.931	0.94	0.865
RQA Trend EMD-filtered	0.793	0.944	0.801	0.886

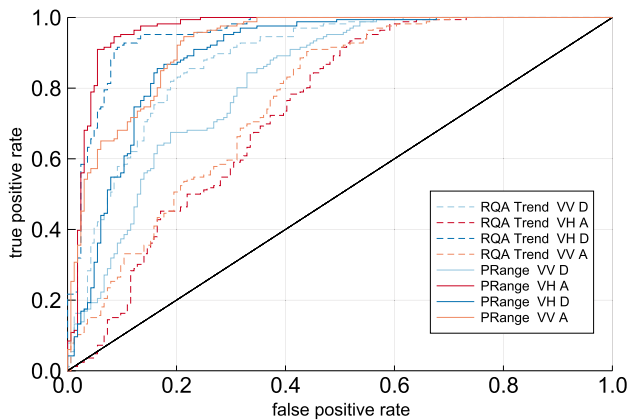


Fig. 9. ROC for the labeling of deforestation against stable forest for the PRange and RQA Trend in Kiuc.

ascending data is best and all other combinations are similar to each other.

Fig. 9 shows the ROC curves for the Kiuc test site. Here the RQA Trend metric and the PRange are similar in separating between stable forest and deforestation although with different underlying datastacks. For the RQA Trend, the best combination is the VH descending data and for the PRange, it is the VH ascending data.

IV. DISCUSSION

Since deforestation leads to a drop in backscatter, the PRange and the RQA Trend both succeed in separating deforestation from stable forest areas in Sentinel-1 C-Band SAR data. The deforested areas in our test sites are changed into a land cover with a highly seasonal backscatter signal with maxima which are as high as the backscatter from stable forest (see Fig. 3). This leads to misclassifications of old deforestation as new deforestation in the PRange. The RQA Trend is not so prone to these seasonality effects and thus can distinguish between old and new deforestations. Thus, RQA Trend provides additional information such as the time of deforestation, which might be a valuable parameter within the REDD+ framework.

Furthermore, the orbit influences the separability between forest and deforestation. Stable forest features a lower backscatter in the descending orbit than in the ascending orbit and deforested areas feature a higher backscatter in the descending orbit than in the ascending orbit. These influences on the backscatter intensity lower the difference between stable forest and deforested areas in the descending orbit. The differences in backscatter intensity between the orbits are visible not only for single deforestations but over the whole region and in different angles to the satellite. Therefore, a different looking angle cannot explain this observation. Since geometric changes on the ground would be visible in both ascending and descending orbit, we conclude that these differences are caused by regular changes in the dielectric properties of the land cover. The ascending and descending orbits differ by the acquisition time. The descending orbit images are acquired at 7:30 A.M. and the ascending orbit images are acquired at 7:40 P.M. local time. This difference in the acquisition time is presumably connected to differences in the water content on and in the vegetation caused by the diurnal water cycle. In our case, the PRange metric performs best with VH ascending data for both test sites, whereas the RQA Trend shows a different behavior in the two test sites. Since the water cycles are different for different biomes, the best possible orbit has to be selected for the monitored biome and climate region. The influence of the acquisition time on the mapping accuracy should be further investigated in future studies.

We utilized the EMD-filter to reduce the influence of speckle. This filter is only applied to the temporal domain and therefore does not diminish the spatial resolution. It reduces the temporal variance in the backscatter signal for the forested and the deforested areas and therefore decreases the overall PRange values. However, it decreases the PRange values of forest by a larger amount than the PRange values for deforestations. Thus, the filtering had a positive impact on the separability between deforestation and stable forest.

In contrast to other approaches of deforestation mapping with Sentinel-1, we do not aspire to map the deforestations in near real time rather to produce yearly or biennially maps with the best possible spatial resolution. Since the introduced approach uses the full time series and its order, we can incorporate the seasonality of the forest signal in our change detection algorithm. It also accomplishes to map small-scale deforestations. The

mapping accuracy is comparable to the approaches reported in [8]–[10]. The derived deforestation information can be updated yearly and can be used in measurement reporting and verification systems for the REDD+ process.

V. SUMMARY AND CONCLUSION

We investigated the use of multitemporal metrics of hypertextual Sentinel-1 backscatter time series to separate stable forest from deforestation. We compared the RQA Trend metric to the range between the 5th and the 95th multitemporal percentile. To the best of our knowledge, this is the first time that RQA has been applied on SAR data and the first thorough investigation of the separation capabilities of the PRange. Both methods are suited to separate between stable forest and deforestation. The PRange provides a better separability between stable forest and new deforestation. The RQA Trend metric on the other hand detects the time of the deforestation. We tested the separability at two test sites in Mexico. One test site is a temperate forest area in central Mexico, and the other is a tropical dry forest area in Yucatan. We observed an impact of the orbit on the separability of deforestations and assume that this observation is due to the different water contents during the acquisition times. In the temperate forest, the VH ascending PRange separates best between deforestation and forest. For dry forest, the results are not as conclusive. Therefore, we suggest that the best combination of polarization, acquisition time, and algorithm must be detected separately for every biome.

This study demonstrates the great potential of RQA on Sentinel-1 time series for the detection of deforestations in the semitropics. In future work, this metric should be used to derive deforestation maps for larger areas. Nevertheless, further investigations are needed to quantify the impact of the parameters of the RPs on the RQA metric computation. These parameters could be revised for the detection of deforestations. From the RP of a time series, other metrics can be computed. These metrics should be examined for the tasks of land cover and land cover change classification.

ACKNOWLEDGMENT

This work uses Copernicus Sentinel data 2017–2019. The authors would like to thank the editor and the anonymous reviewers for their comments to improve the quality of the article. They would like to thank the European Space Agency, ESA, for funding the Earth System Data Lab, ESDL.

REFERENCES

- [1] Y. Pan *et al.*, “A large and persistent carbon sink in the world’s forests,” *Science*, vol. 333, no. 6045, pp. 988–993, Aug. 2011. [Online]. Available: <https://science.sciencemag.org/content/333/6045/988>
- [2] G. B. Bonan, “Forests and climate change: Forcings, feedbacks, and the climate benefits of forests,” *Science*, vol. 320, no. 5882, pp. 1444–1449, Jun. 2008. [Online]. Available: <https://www.sciencemag.org/lookup/doi/10.1126/science.1155121>
- [3] M. C. Hansen *et al.*, “High-resolution global maps resolution global maps of 21st-century forest cover change,” *Science*, vol. 342, no. 6160, pp. 850–853. [Online]. Available: <https://science.sciencemag.org/content/342/6160/850>
- [4] M. Shimada *et al.*, “New global forest/non-forest maps from ALOS PALSAR data (2007–2010),” *Remote Sens. Environ.*, vol. 155, pp. 13–31, 2014. [Online]. Available: <http://www.sciencedirect.com/science/article/pii/S0034425714001527>
- [5] M. Martone, F. Sica, C. Gonzalez, J.-L. Bueso-Bello, P. Valdo, and P. Rizzoli, “High-resolution forest mapping from tandem-x interferometric data exploiting nonlocal filtering,” *Remote Sens.*, vol. 10, no. 9, 2018. [Online]. Available: <https://www.mdpi.com/2072-4292/10/9/1477>
- [6] A. Bouvet, S. Mermoz, M. Ballre, T. Koleck, and T. Le Toan, “Use of the SAR shadowing effect for deforestation detection with Sentinel-1 time series,” *Remote Sens.*, vol. 10, no. 8, Aug. 2018, Art. no. 1250. [Online]. Available: <http://www.mdpi.com/2072-4292/10/8/1250>
- [7] M. Rüetschi, D. Small, and L. Waser, “Rapid detection of windthrows using Sentinel-1 C-Band SAR data,” *Remote Sens.*, vol. 11, no. 2, Jan. 2019, Art. no. 115. [Online]. Available: <http://www.mdpi.com/2072-4292/11/2/115>
- [8] K. Shimizu, T. Ota, and N. Mizoue, “Detecting forest changes using dense Landsat 8 and Sentinel-1 time series data in tropical seasonal forests,” *Remote Sens.*, vol. 11, no. 16, Jan. 2019, Art. no. 1899. [Online]. Available: <https://www.mdpi.com/2072-4292/11/16/1899>
- [9] J. Reiche, E. Hamunyela, J. Verbesselt, D. Hoekman, and M. Herold, “Improving near-real time deforestation monitoring in tropical dry forests by combining dense Sentinel-1 time series with Landsat and ALOS-2 PALSAR-2,” *Remote Sens. Environ.*, vol. 204, pp. 147–161, Jan. 2018. [Online]. Available: <https://linkinghub.elsevier.com/retrieve/pii/S0034425717304959>
- [10] M. Hirschmugl, J. Deutscher, K. Gutjahr, C. Sobe, and M. Schardt, “Combined use of SAR and optical time series data for near real-time forest disturbance mapping,” in *Proc. 2017 9th Int. Workshop Anal. Multitemporal Remote Sens. Images (MultiTemp)*, Jun. 2017, pp. 1–4.
- [11] J. Kellndorfer, “Using SAR data for mapping deforestation and forest degradation,” in *Synthetic Aperture Radar (SAR) Handbook: Comprehensive Methodologies for Forest Monitoring and Biomass Estimation*, A. I. Flores-Anderson, K. E. Herndon, R. B. Thapa, and E. Cherrington, Eds., Huntsville, AL: SERVIR Global Science Coordination Office National Space Science and Technology Center, 2019. [Online]. Available: https://gis1.servirglobal.net/TrainingMaterials/SAR/SARHB_FullRes.pdf
- [12] J. P. Zbilut and C. L. Webber, “Embeddings and delays as derived from quantification of recurrence plots,” *Phys. Lett. A*, vol. 171, no. 3, pp. 199–203, 1992. [Online]. Available: <http://www.sciencedirect.com/science/article/pii/037596019290426M>
- [13] J.-P. Eckmann, S. O. Kamphorst, and D. Ruelle, “Recurrence plots of dynamical systems,” *Europhys. Lett.*, vol. 4, no. 9, 1987, Art. no. 973. [Online]. Available: <http://stacks.iop.org/0295-5075/4/i=9/a=004>
- [14] S. Li, Z. Zhao, and F. Liu, “Identifying spatial pattern of NDVI series dynamics using recurrence quantification analysis: A case study in the region around Beijing, China,” *Eur. Phys. J.*, vol. 164, no. 1, pp. 127–139. [Online]. Available: <http://www.springerlink.com/index/10.1140/epjst/e2008-00839-y>
- [15] N. Marwan, J. Kurths, and S. Foerster, “Analysing spatially extended high-dimensional dynamics by recurrence plots,” *Phys. Lett. A*, vol. 379, no. 10–11, pp. 894–900. [Online]. Available: <https://linkinghub.elsevier.com/retrieve/pii/S0375960115000742>
- [16] N. Marwan, M. C. Romano, M. Thiel, and J. Kurths, “Recurrence plots for the analysis of complex systems,” *Phys. Rep.*, vol. 438, no. 5, pp. 237–329, 2007. [Online]. Available: <http://www.sciencedirect.com/science/article/pii/S0370157306004066>
- [17] G. Datsis, “Dynamicalsystems.jl: A julia software library for chaos and nonlinear dynamics,” *J. Open Source Software*, vol. 3, no. 23, Mar. 2018, Art. no. 598. [Online]. Available: <https://doi.org/10.21105/joss.00598>
- [18] J. Rzedowski and X. Madrigal-Sanchez, “Excursion from the centre to Northeast: Itinerary tampico zacualtipan,” (in spanish), in *Proc. Latin Amer. Congress Botany. Botanical Tour Guides Mexico*, 1972, pp. 237–242.
- [19] J. L. Hernández-Stefanoni *et al.*, “Improving species diversity and biomass estimates of tropical dry forests using airborne LiDAR,” *Remote Sens.*, vol. 6, no. 6, pp. 4741–4763, 2014. [Online]. Available: <https://www.mdpi.com/2072-4292/6/6/4741>
- [20] G. Krieger *et al.*, “Tandem-x: A satellite formation for high-resolution SAR interferometry,” *IEEE Trans. Geosci. Remote Sens.*, vol. 45, no. 11, pp. 3317–3341, Nov. 2007.
- [21] E. García de Miranda, *Modifications to the Koppen Climate Classification System: To Adapt it to the Conditions of the Mexico* (in spanish), 4th ed. México: UNAM, Institute of Geography, 1981.

- [22] F. Paz, "Geo-FCT validation/calibration sites for Mexico," COLPOS, Montecillo, Estado de Mexico, Mexico, 2009.
- [23] M. D. Soriano-Luna *et al.*, "Determinants of above-ground biomass and its spatial variability in a temperate forest managed for timber production," *Forests*, vol. 9, no. 8, 2018, Art. no. 490. [Online]. Available: <https://www.mdpi.com/1999-4907/9/8/490>
- [24] National Weather Service, "Monthly temperature and rainfall summaries," (in spanish). [Online]. Available: <https://smn.conagua.gob.mx/es/climatologia/temperaturas-y-lluvias/resumenes-mensuales-de-temperaturas-y-lluvias>
- [25] T. Urquiza-Haas, P. M. Dolman, and C. A. Peres, "Regional scale variation in forest structure and biomass in the Yucatan peninsula, Mexico: Effects of forest disturbance," *Forest Ecol. Manage.*, vol. 247, no. 1, pp. 80–90, 2007. [Online]. Available: <http://www.sciencedirect.com/science/article/pii/S0378112707003325>
- [26] R. Birdsey *et al.*, "Network of intensive carbon monitoring sites in Mexico: Multi-institutional collaboration to support Mexico's National MRV/REDD+ systems and North American carbon cycle research," [Online]. Available: https://www.nacarbon.org/meeting_ab_presentations/2015/2015_Poster_Birdsey_47_224.pdf
- [27] J. Truckenbrodt *et al.*, "Towards Sentinel-1 SAR analysis-ready data: A best practices assessment on preparing backscatter data for the cube," *Data*, vol. 4, no. 3, Jul. 2019, Art. no. 93. [Online]. Available: <https://www.mdpi.com/2306-5729/4/3/93>
- [28] NASA Shuttle Radar Topography Mission United States 1 arc second. Version 3. 20 °N 98 °W. NASA EOSDIS Land Processes Distributed Active Archive Center (LP DAAC), Sioux Falls, SD, USA, 2013. [Online] Available: <http://dx.doi.org/10.5067/MEaSUREs/SRTM/SRTMUS1.003>
- [29] D. Small, "Flattening gamma: Radiometric terrain correction for SAR imagery," *IEEE Tran. Geosci. Remote Sens.*, vol. 49, no. 8, pp. 3081–3093, Aug. 2011.
- [30] "ESA snap—ESA Sentinel application platform," [Version 6.0.2]. [Online]. Available: <http://step.esa.int>
- [31] J. Truckenbrodt, F. Cremer, I. Baris, and J. Eberle, "pyroSAR: A framework for large-scale SAR satellite data processing," in *Proc. Conf. Big Data Space*, P. Soille, S. Loekken, and S. Albani, Eds., Luxembourg: Publications Office of the European Union, 2019, pp. 197–200.
- [32] M. D. Mahecha *et al.*, "Earth system data cubes unravel global multivariate dynamics," [Online]. Available: <https://www.earth-syst-dynam-discuss.net/esd-2019-62/>
- [33] F. Cremer, M. Urbazaev, C. Berger, M. Mahecha, C. Schmullius, and C. Thiel, "An image transform based on temporal decomposition," *IEEE Geosci. Remote Sens. Lett.*, vol. 15, no. 4, pp. 537–541, Apr. 2018.
- [34] S. Quegan and J. J. Yu, "Filtering of multichannel SAR images," *IEEE Trans. Geosci. Remote Sens.*, vol. 39, no. 11, pp. 2373–2379, Nov. 2001.



Felix Cremer received the Diploma in mathematics from the University of Leipzig, Leipzig, Germany, in 2014. In 2015, he joined the Department for Earth Observation, Friedrich Schiller University of Jena, to work on his Ph.D. study.

In 2019, he joined the German Aerospace Centre (DLR) Institute of Data Science, Jena, Germany. His research focuses on nonlinear methods for the analysis of irregular time series, which he applies for the analysis of radar time series for forest applications.



Mikhail Urbazaev (Member, IEEE) received the Ph.D. degree from the Friedrich Schiller University of Jena, Jena, Germany, in 2019.

His Ph.D. work dealt with the estimation of vegetation structure parameters in Mexico from satellite imagery. Since 2014, he has been with the Department for Earth Observation, University of Jena, as a Research Assistant. His research focuses on the synergistic use of synthetic aperture radar, LiDAR, and optical data for estimation of aboveground biomass and vegetation structural parameters as well as on

time series analysis for mapping of forest and water dynamics.



José Cortés is currently working toward the Ph.D. degree with Friedrich Schiller University, Jena, Germany.

His research focuses on spatio-temporal trend detection in environmental data.

Mr. Cortés is a member of the International Max Planck Research School on Global Biogeochemical Cycles (IMPRS-gBGC), a joint program with the Max Planck Institute for Biogeochemistry.



John Truckenbrodt received the B.Sc. degree in geography and the M.Sc. degree in geoinformation science from the Friedrich-Schiller-University Jena (FSU), Jena, Germany, in 2012 and 2015, respectively.

Since 2015, he has been a Researcher with the Department for Earth Observation, FSU, and since 2019, in parallel, as a Researcher with the German Aerospace Centre (DLR) Institute of Data Science, Jena, Germany. His main research focus is the analysis of synthetic aperture radar time series for hydrology applications with a strong focus on the development of automated processing chains and data cube solutions.



Christiane Schmullius received the M.A. degree in geography/remote sensing from the University of California, Santa Barbara, Santa Barbara, CA, USA, in 1986, as an ITT and Fulbright Fellow, and the Ph.D. degree from the Institute of Space Sciences, Free University Berlin, Berlin, Germany, in 1991.

Her doctoral work focused on radar remote sensing of agricultural crops. From 1991 to 2000, she led the "Geomatics"-Group at the Institute for Radar Systems of the German Aerospace Center, DLR. In 1994, she coordinated the SIR-C/X-SAR Science Team and in 2000 became DLR's Project Scientist for the Shuttle Radar Topography Mission. She has coordinated several European Commission Projects in Siberia, especially on radar interferometry applications for vegetation structure mapping. Since 2000, she has been a Professor with the Department for Earth Observation, Friedrich Schiller University Jena, Jena, Germany, where she is focusing on synergistic optical-radar applications for large-scale land surface mapping.

Prof. Schmullius is a member of the following panels: Earth Science Advisory Committee of the European Space Agency, Space Advisory Group to the European Commission, and European Space Science Council of the European Science Foundation.



Christian Thiel received the Ph.D. degree (with Hons.) in 2004 and the Habilitation degree, in 2014 from the Friedrich Schiller University (FSU), Jena, Jena, Germany.

The topic of his Ph.D. work was the investigation of polarimetric and interferometric airborne SAR data for the derivation of biophysical parameters. The subject of his Habilitation thesis was radar remote sensing over forest. Between 2004 and 2018, he was a Research Project Assistant with the FSU Jena and was involved in various projects. He is also involved in the

Kyoto and Carbon Initiative, dealing with large-area PALSAR data applications focusing on forest. Since 2018, he has been with the German Aerospace Center (DLR), Jena, Germany. His research interests include the synergistic usage of optical and SAR-data for landcover classification, earth observation in support for transboundary aquifer management, utilization of JERS-1 SAR-data for forest cover detection, and the operationalization of earth observation-based forestry applications.